The Scanning Problem of FLARE and THz Pulse Slicing

Milo Vermeulen

Primary supervisor: Prof. dr. W.J. van der Zande
Secondary supervisors: Dr. R. T. Jongma, Dr. D. Arslanov, Dr. Vitali Zhaunerchyk

August 31, 2014

FELIX Facility
Radboud University Nijmegen

Abstract

This bachelor internship report deals with operational aspects of FLARE, a terahertz Free Electron Laser. It reports on calculations on the propagation of light in the cavity of FLARE in a search for the origin of so-called gaps in the scanning range of the laser. These gaps were not anticipated in its original design and the origin of this phenomenon is still unclear. This report also describes a method of transforming the output of FLARE, which is prescribed by the operational mechanism, into pulses of a certain length and shape. This process uses laser driven switchable mirrors to select light pulses of tunable length. The efficiency of this process has been quantified. It is concluded that a set-up based on silicon-on-insulator mirrors will be able to perform the desired pulse slicing.

Contents

1   Introduction

FLARE (Free-electron Laser for Advanced spectrocopy and high-Resolution Experiments) is one of the terahertz free-electron lasers (henceforth FELs) that operate at the Radboud University in Nijmegen. Funds for the project were received in 2006 and first lasing was achieved five years later in september of 2011. FELs are elegant in that they work over the full range of the electromagnetic spectrum, their exact wavelength range depending on their design. While they would be inferior to other types of lasers in the visible and ultraviolet range where atomic transitions make for excellent laser-light generation, for instance, their operation is left relatively unopposed in the terahertz range. The so-called THz-gap that exists between the efficient operation of photonics on one hand and electronics on the other is thus an ideal playground for these machines. Another advantage of the FEL is its ability to scan continuously over a range of wavelengths while lasers depending on atomic transitions are bound to the properties of their gain medium.

The FEL consists, in essence, of an electron source, accelerator and a laser cavity that envelops a magnetic structure. The electron source and accelerator only serve to produce bunches of relativistic electrons: FLARE can accept electron bunch trains at a production rate of 3 GHz, but recently 20 MHz electron bunch trains have also been produced and successfully injected into the magnetic structure. These electrons have a kinetic energy of 10, 15 or 16 MeV depending on the desired wavelength of produced light. The magnetic structure of a FEL is called an undulator and in the case of FLARE, it consists of two rows of permanent magnets that produce a periodic magnetic field (see figure 1).

The relativistic electron bunches travel between these rows and produce a periodic 'wiggling' motion per the Lorentz force. The first bunches travelling through the undulator emit relatively weak radiation due to different parts of the electron bunch emitting at a different phase. Eventually a single phase gains a slightly higher intensity by chance and stimulates a microbunching effect that further reinforces the dominance of the specific phase. This is, briefly summarised, the gain effect of the FEL. The spacing between microbunches depends on the spontaneously produced wavelength and, by extension, the intial wiggling motion of the electrons. The magnetic field strength of the undulator together with the undulator period and electron energy thus determine in first order the wavelength of the produced radiation in accordance to:

$$\lambda \approx \frac{l_0}{2\gamma^2}(1 + K^2) \tag{1}$$

Here, λ is used to signify the produced radiation, l_0 the undulator period, γ the relativistic gamma-factor of the electrons ($\gamma = [1 - v^2/c^2]^{-1/2}$) and K the undulator parameter which is dependent on the magnetic field and period of the undulator. Commonly, the undulator parameter (more specifically the magnetic field strength) is varied in order to create a range of wavelengths. For a full analysis of the FEL gain mechanism, please refer to *Aspects of Short Pulse Free Electron Lasers and Spontaneous Coherence* which was written as the first part of this bachelor internship with the help of [7] and [12].
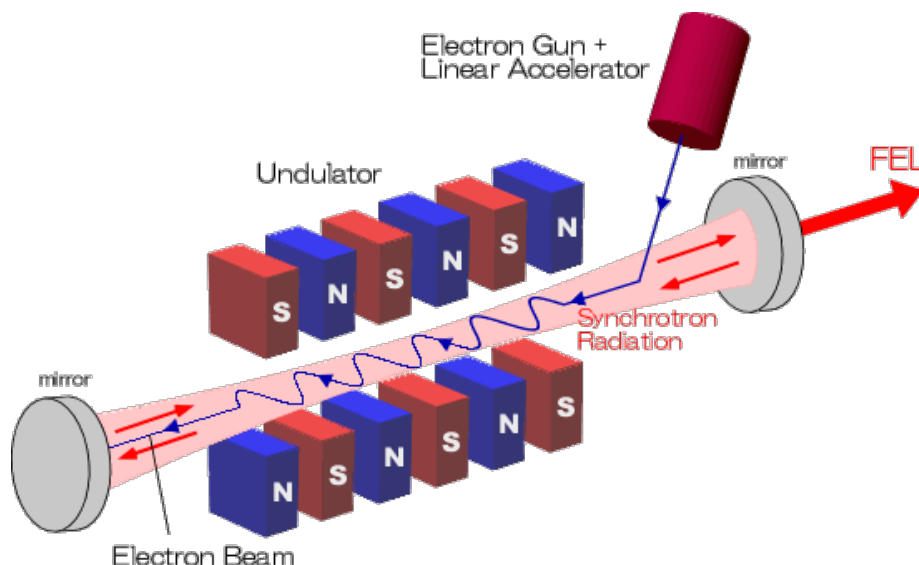

Figure 1: A schematic overview of a FEL.[4]

One part of this bachelor internship report will entail the investigation into the gaps that appear in the spectrum of FLARE. Since it came into operation, FLARE has only been able to lase at certain specific wavelengths, effectively negating one of the main advantages of the FEL.
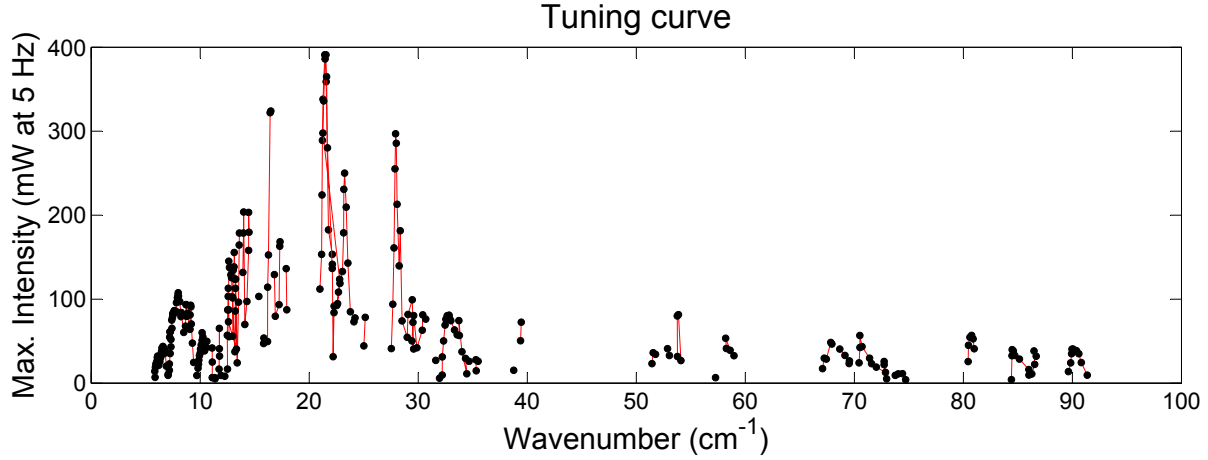

Figure 2: FLARE radiation intensity graphed against wavenumber. Note that any sign of radiation lacks at many points in the figure.

The erratic behaviour of the tuning curve has made it difficult to discern the origin of the resulting gaps. In this bachelor internship, spontaenous emission and lasing of FLARE have been observed both in the frequency and in the time domain. Additionally, it was investigated whether the shape of the electron bunches could cause destructive interference in spontaneous emission. That is, in the so-called first pass, when the laser cavity is still empty of radiation and the first electron bunch enters.

The second part of this bachelor internship entails the temporal shaping of FLARE's pulses. These are, in the case of FLARE, 2-15 μs long [6], proving too long for certain dynamic experiments. It is not possible to make FLARE's pulses shorter with the current required start-up time of the electron accelerator, making it necessary to alter them after they have been produced. This can be done with the use of plasma mirrors: semiconductor slabs of varying thickness. In the experiments carried out, silicon slabs of 5 and 20 μm were used, as well as a slab consisting completely of silicon, approximating infinite thickness. The slabs were coated in anti-reflection coating to minimise unwanted reflection effects.

The silicon is normally transparent to FLARE's light, but electrons can be excited in its surface and bulk, creating a plasma that reflects THz radiation. Excitation is induced by the use of a second, short-pulse laser. The plasma decays depending on the properties of the slab as well as the semiconductor material and purity, electrons in the plasma being able to recombine with the help of defects and impurities. Experiments have been conducted on these slabs in the past, examining their behaviour in an attempt to catch it in a simulation model. These experiments were carried out using a pyroelectric detector which is very sensitive, but does not work on short enough timescales to accurately measure the temporal evolution of the plasma. In this bachelor internship, the behaviour of the plasma mirrors was characterised by a much faster photodiode, allowing for a direct comparison between the simulation model and reality.

2 Method FLARE

The Initial Situation In order to change the output wavelength of a FEL, two parameters have to be modified. The first is the undulator parameter K as described in equation 1. More accurately, the distance between the rows of permanent magnets is altered, changing the intermediate magnetic field and making the wiggling motion of the electrons stronger or weaker. The second parameter that is to be changed is the cavity length, which is to act as a resonating cavity when properly adjusted.

An intuitive way to visualise FLARE's scanning gaps is to map output intensity as both a function of the undulator parameter and cavity length, shown in figure 3. The expected graph would have run along the now-isolated islands continuously, curved slightly because of waveguide dispersion effects. Instead, large gaps are present and it can be noted that there are very few positions in the graph at which FLARE works at full power. Evidently, something changes along the border of these islands that causes FLARE to start and stop lasing. Examining these borders might yield a better understanding in the scanning problem of FLARE.
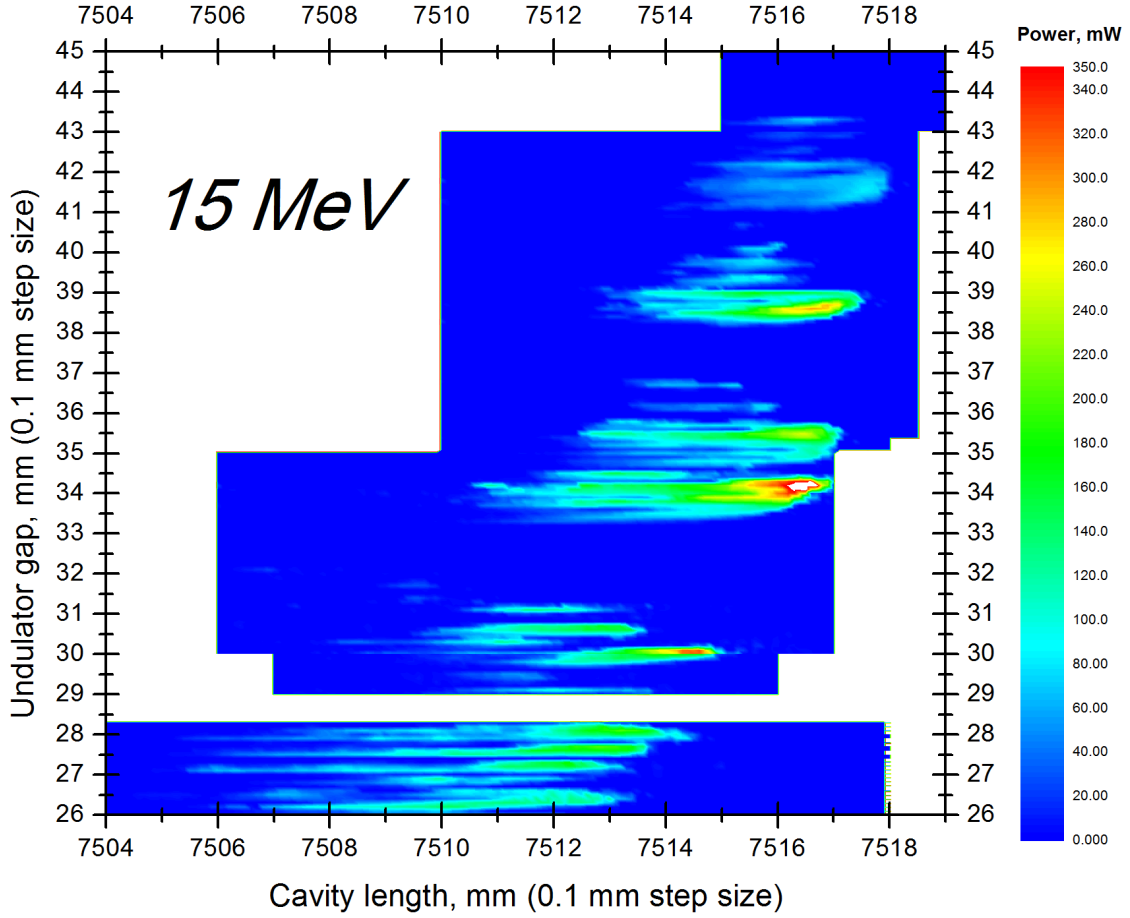

Figure 3: The total map of FLARE lasing intensity as a function of undulator gap and cavity length. A continuous band is expected along the line where there are now merely islands. Thanks to dispersion effects within the waveguide, the cavity length needs to have a different value for different wavelength in order to make light pulses meet up with electron pulses on consecutive roundtrips. The fact that the islands do not form a perfectly diagonal line is a testament to nonlinear waveguide dispersion effects. Additionally, it can be noted that the islands are rather long in the cavity length direction. This suggests that lasing can still occur when the radiation pulses only partially overlap with subsequent electron pulses, though the output intensity is strongly diminished in this case.

Time-Domain Analysis   A preliminary analysis of FLARE's pulses was made in the time domain. To this end, the intensity of emitted light was determined as a function of time with a resolution sufficient to resolve the general structure of FLARE's radiation pulses. The pulses were recorded using either a bolometer or a pyroelectric detector, depending on the intensity of the light. Since only a small number of averages were required per setting, a single FLARE pulse profile was recorded extremely quickly and a scan could be performed over both the undulator gap and cavity length, albeit not simultaneously. These pulse profiles could then be visually presented in a contour graph where intensity is graphed against time and either undulator gap or cavity length. While it was not expected that this would show major new insights, it could help gain a better understanding of the electron bunch profile as it goes through the undulator.

Time-domain analysis was also performed on purely spontaneous emission: emission by electrons not influenced by already circulating light. It was hereby attempted to link the spontaneous pulse profile to the ability of FLARE to lase using those settings. The only viable scan that could be made in this situation was the variation of the undulator gap: the laser cavity was disabled to receive purely spontaneous emission and so a scan of the cavity length would have been irrelevant.

Michelson Interferometer   The goal of this specific experiment was to observe and characterise both spontaneous and coherent emission of FLARE. To this end, a Michelson interferometer was constructed that could operate regardless of the intensity of the light passing through it. It consisted of a beamsplitter going into two arms, each with a mirror at its end: one that was more or less fixed but could be slightly adjusted for calibration, and one on a motor stage. When the two mirrors are equally far from the beamsplitter, light will cause positive interference at the intersection point upon returning from the two arms. When the path length between the arms differs by half a wavelength, however, returning light pulses will be exactly out of phase and destructively interfere. These processes repeat after an entire wavelength and so an interferogram is created by slowly varying one mirror's distance from the beamsplitter.
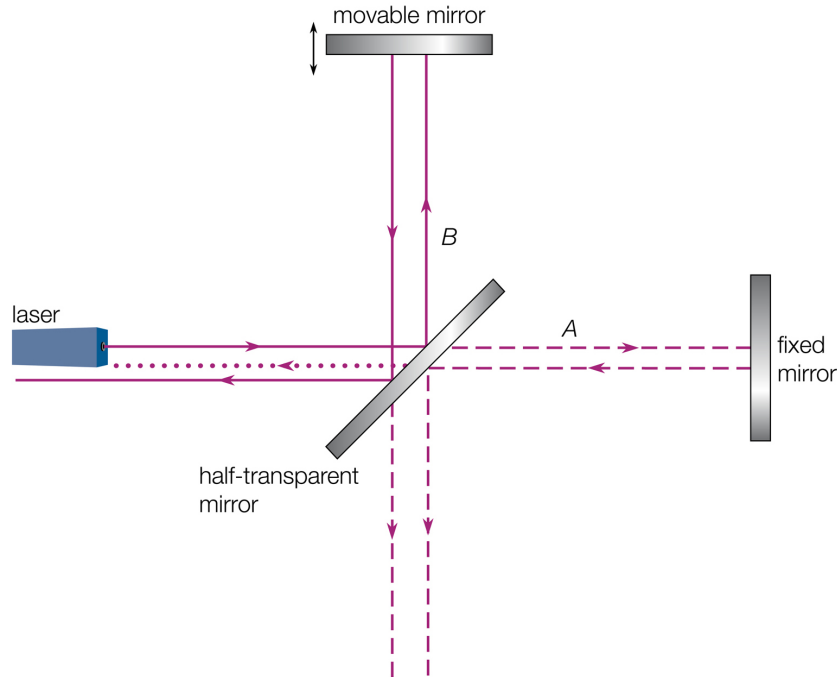

Figure 4: The schematic layout of a typical Michelson interferometer. The returning and recombined light beams have been drawn separately for clarity: in reality these would have to overlap on the detector (not included here, but present off the bottom of the figure) in order to cause interference.[2]

The components of the interferometer were aligned using a HeNe laser and interference of this laser could indeed be observed under careful adjustment. The laser did not prove consistent enough to produce stable interference when the arm lengths were far apart, however, causing some confusion regarding the alignment of the interferometer. The interferometer motor-arm was made to move in steps of 33 μm, allowing for high-resolution interferograms. While this small step size allowed for good results, it did

greatly increase the time it takes to complete a complete scan, especially when combined with the fact that many averages are required at a singular position to acquire a smooth signal.

Undulator parameters and cavity lengths were varied, performing spectral analysis using the interferometer in lasing positions, in lasing gaps and on the border of the lasing islands. In essence, these different positions were examined in order to try and discern where the scanning problem lies. This is made more difficult by the fact that different instruments have to be used for spontaneous emission and lasing. A hardy pyroelectric detector was used to measure lasing and a sensitive bolometer observed FLARE's spontaneous emission. Using the wrong type of detector could result in data-loss, or worse, damaging the bolometer.

In order to purely observe FLARE's spontaneous emission, all cavity effects needed to be extinguished. In order to achieve this, the moveable downstream mirror was put in a position very far from resonance. In later experiments it was blocked as well and later on completely removed out of fear that cavity effects were still causing interference via an unknown mechanism. In the case of spontaneous emission, the interferometer exited directly into a bolometer. This instrument proved to be fast and sensitive enough to observe a temporal profile of each pulse that came out of the interferometer, creating an interferogram at each point on the pulse. For the main analysis, certain areas of the pulse were averaged and their interferograms were transformed into the spectral domain via a fast Fourier-transform (henceforth FFT).

Theoretical Analysis of Waveguide Dispersion FLARE is outfitted with a waveguide that reaches all the way to the mirrors of the laser cavity, preventing radiation losses that would otherwise occur due to mode-conversion when radiation would enter or exit the waveguide. It was installed to contain radiation within the laser cavity: diffraction would otherwise cause the laser beam to blow up far beyond the dimensions of the cavity mirrors.[8] The waveguide consists of two metallic parallel plates 10 mm apart and perpendicular to the undulator magnetic field. Standing waves between the waveguide plates appear, making sure that only some modes can resonate.

The resonator cavity created by the waveguide and mirrors allows for a specific selection of frequencies that can be created within it. A formula for these frequencies is given as follows [3]:

$$\nu_{n,m} = \frac{c\gamma_z^2 \beta_z \epsilon_m}{l_0} \left(1 \pm \beta_z \sqrt{1 - \left(\frac{n l_0}{2 b \gamma_z \beta_z \epsilon_m} \right)^2} \right) \quad , \quad \epsilon_m = 1 - (m + 1/2)/k_0 z_r \tag{2}$$

The formula has γ_z and β_z as the gamma-factor and velocity (relative to the speed of light) of the electrons in the direction of the undulator, c as the speed of light and b as the separation between the waveguide plates. The variable ϵ_m is defined by $k_0 = 2\pi/l_0$ and z_r is the Rayleigh length of the beam. It has to be noted that γ_z is not considered constant, as it is actually defined by $\gamma/\sqrt{1 - K^2}$ [7] where K is the undulator parameter which can actively be varied, effectively changing the possible frequencies. By varying the electron energy, γ_z can be varied as well, discontinuously. This changes β_z as well, though the change in this factor is negligible.

Finally, the indices m and n can take on any positive integer, only a few of which are relevant. They describe the electromagnetic wave inside the waveguide: m signifies its order of Hermite-Gaussian modulation and n concerns the mode of the wave between the waveguide plates. The latter can be visualised as standing waves between the plates, $n = 1$ being the fundamental or first harmonic. It follows that only odd harmonics will be sustained within the cavity, as even harmonics are antisymmetric and cause destructive interference with centred electron bunches.

The main point of this portion of the project was to examine the dependence of the ouput frequency on the undulator parameter K. Discrete changes to m, n and γ (or the electron kinetic energy E_k, more accurately) can then be made to see how the K dependence of the output frequency shifts.

Theoretical Analysis of the Electron Bunch Shape Initially, it was theorised that interbunch interactions in FLARE's undulator could not be neglected. The standard bunch repetition of 3GHz simply placed the bunches too close to each other to them separately. For comparison, the undulator length is 4.4 m while such a repetition rate would create bunches around 10 cm apart. This means that there are multiple bunches in the undulator at the same time, possibly causing disruptive effects. The bunches are not perfectly square, after all, and parts of one bunch could overlap with the next. To find out what effects might stop lasing from occurring, advanced simulations using many bunches in one undulator had been conducted in the past.

Recently, a bunch repetition rate of 20MHz has been achieved, spacing them 15 m apart and thus allowing no more than one bunch to be in the undulator at any given time. This rate was chosen because it places the electron bunches two cavity lengths apart, allowing generated light to travel around the cavity and intercept the next electron bunch. Any lower bunch repetition rate would require light to travel around the laser cavity more than once in order to encounter the next electron bunch with increased cavity losses. With the bunches spaced much farther apart than in the previous 3 GHz case and the scanning gaps still persisting, it became obvious that interbunch effects were not the main problem and thus simulations could be simplified to viewing a single bunch in the undulator.

In this bachelor internship, a very simple model has been used to analyse the effects of bunch shape on spontaneous emission. To this end, it is assumed that all electrons fly perfectly through the centre of the undulator with no Coulomb forces or pre-existing radiation present. Two kinds of radiation emission play a role in this simplified version of spontaneous emission of FLARE. These are incoherent and coherent emission, and they are characterised by their generation processes. Incoherent emission arises from random fluctuations in the electron beam distribution and coherent emission from fluctuations on a scale relative to the generated wavelength. The former is proportional to the amount of electrons and the latter is proportional to its square. The total power can then be described by the following formula [5]:

$$P(k) = NP_1 + N^2 P_1 f(k) \tag{3}$$

Here, N describes the amount of electrons and P_1 is the power each one provides individually. The first term in the equation signifies the power produced by incoherent emission and is more or less self-explanatory. The second term stands for the coherent emission and includes a form factor which can be described as

$$f(k) = \left| \int \exp(ikz) S(z) \mathrm{d}z \right|^2 \tag{4}$$

Where $S(z)$ is the longitudinal density distribution of the electron beam and $k = k_s - k_0 \approx k_s$ is the difference between the radiation wave vector and the undulator wave vector ($k_0 = 2\pi/l_0$). $f(k)$ is directly dependent on $S(z)$ and the form factor will thus change as the density distribution of the electrons is modified. Simple electron bunch shapes can be analysed and their power output can be analysed as a function of their frequency ω (or, more accurately, their wave vector k).[5]

3 Method THz Pulse Slicing

FELs in the FIR range have many advantages over other radiation sources in the area, such as tunability and relatively high intensity light. However, they produce inherently long pulses that only allow for static experiments. With extra-cavity modification of the temporal profile of FLARE's pulses, new research areas would open. A shorter pulse or even a number of successive short pulses of FIR light could lead to new insights in numerous scientific areas.

In this project, silicon-on-insulator (henceforth SOI) wafers were used. These consist of a thin layer of silicon atop an insulator, in this case silicon oxide (SiO_2), which is actually a thin 'buried' layer within the wafer. This insulating layer acts as a barrier for charge carriers generated in the uppermost layer of silicon by a 532 nm pulse, confining them to a select area. Silicon oxide is otherwise transparent to FLARE's light and is strongly insulating, making it an effective barricade. In this project, SOI mirrors with a silicon layer thickness of 5 and 20 μm were examined, as well as a bulk silicon wafer lacking a silicon oxide barrier which can be regarded as infinitely thick. A passivation layer was deposited on top of the silicon to further enhance electron excitation and increase carrier concentration within the wafer.

Detection and Laser Testing   In order to properly characterise pulse slicing mirrors, certain tests had to be conducted first. The detector used was a Thorlabs DET10A silicon biased photodetector, reportedly having a rise time of 1 ns.[10] A peak bias voltage of 10 V could be applied, enhancing the detector's rise time and sensitivity. The laser used was a Quanta-Ray INDI-40-10 from Spectra-Physics, a Nd:YAG laser delivering an advertised 200 mJ of 532 nm wavelength pulses at 10 Hz.[9] Multiple reflective neutral density filters were put onto the detector as protection and the laser was fired at the detector. Because of the filters' reflective nature, a beam dump was required. The data was recorded using a fast oscilloscope.

The THz-gap pertains to detection just as well as it does to generation. In this case it is impossible to detect FIR light directly with the fast detector and so FLARE's radiation is characterised by an indirect method. A near-infrared (henceforth NIR) laserbeam is merged with the FIR laser beam and sent through a sideband generation crystal. In this material, sum frequencies are generated. These sum frequencies appear close to the added laser frequency thanks to the THz frequencies being so much smaller than the NIR ones. The sideband frequencies can then be spatially split from the NIR beam in a spectrometer and observed spectrally with a linear CCD array. For this experiment, the CCD array was displaced and the fast detector was put in its place to observe sideband pulses in the time domain rather than the frequency domain. More information on the exact setup can be found in [11].

Experimental Setup   In order to determine the behaviour of the pulse slicing mirrors, a number of factors needed to coincide in the experimental setup. FLARE's THz pulses were focussed on the slicing mirrors over a typical time of 2 to 11 microseconds. During this time, the YAG laser fired its pulse at the area on the plasma switch the THz light would otherwise pass through, making the mirror momentarily reflective. Portions of reflected THz pulses were then focussed into a sideband generation crystal together with a NIR laser. The NIR/sideband beam was then led into the spectrometer where the different frequencies could spatially be separated and the sideband could be observed with the fast detector. In order to be able to focus on the sideband signal, the detector was placed on a steady platform that could be shifted accurately to scan through the range of the spectrometer. The signal was once again recorded with an oscilloscope. See also figure 5 for a schematic overview of the setup.

Comparison to Simulation Models   Early experiments on the pulse slicing mirrors have yielded simulations to roughly fit the data. The model takes constants of nature into account as well as situation-specific values, such as the properties of the plasma-inducing laser, the thickness of the mirror and the recombination rates in its interior as well as on its surface. The program then calculates the charge carrier concentration in the plasma switch as a function of time and depth and determines the time-evolution of its reflectivity for THz light.

The program is written in MathWorks' MATLAB and can easily be edited to compare simulation with experimental results using a few unknown variables. The fitting variables in this case were defect recombination, which depends on the quality of the mirror, and front surface recombination, which signifies the rate at which electrons recombine on the outside edge of the mirror. Recombination processes that are taken into account are Auger recombination, radiative recombination, impurity recombination and surface recombination.
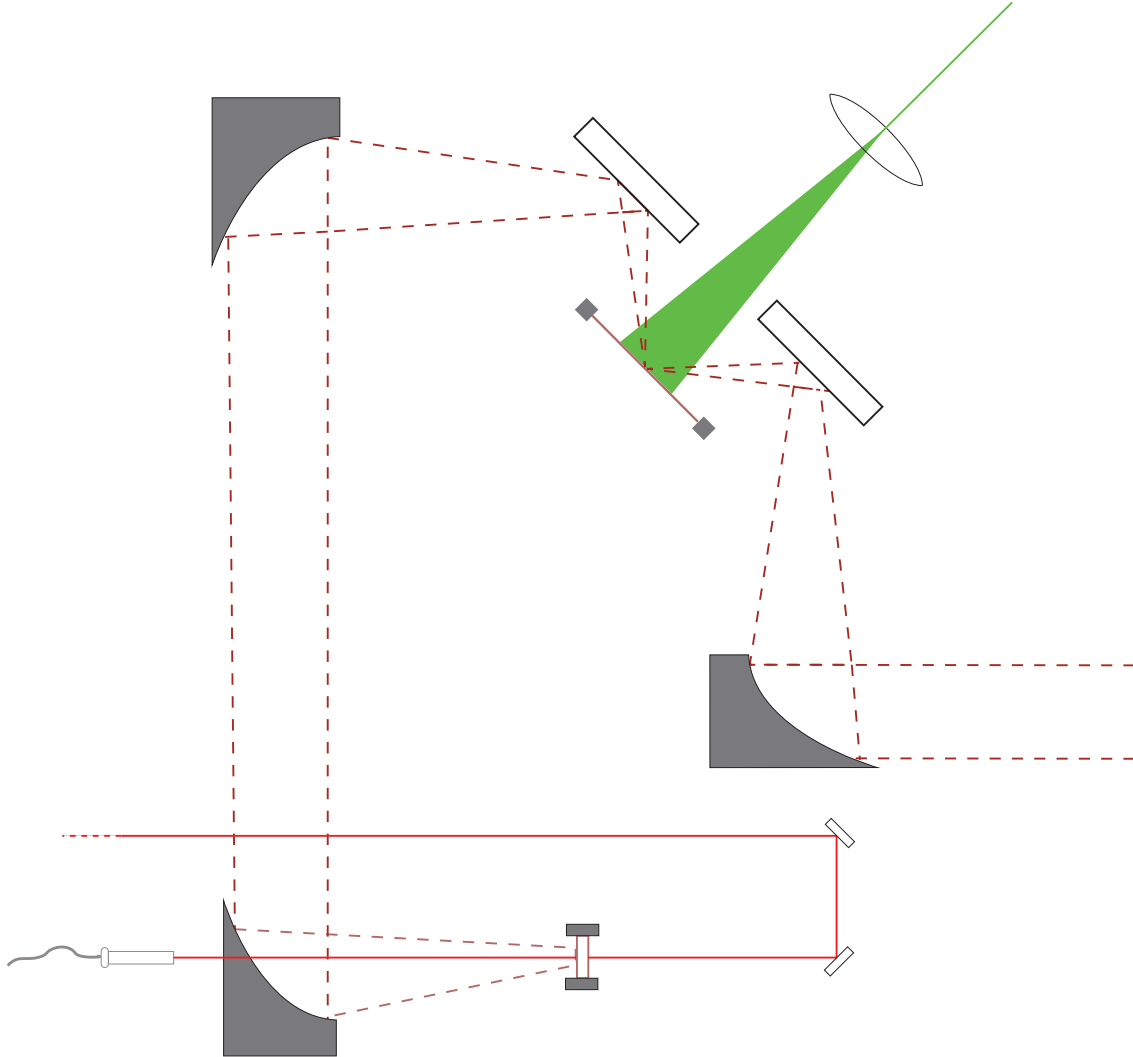
Figure 5: The basic experimental setup of the plasma switch characterisation experiments seen from the top. FLARE's pulses come in from the right and are signified by the thick dotted beam. They are focussed onto the plasma switch, coinciding with a short pulse of 532 nm light coming from a YAG laser. Afterwards, they are sent through a sideband-generating crystal together with a fibre-coupled NIR continuous laser beam. The NIR beam and generated sidebands then travel to the spectrometer (not included in this overview but identical in setup to [11]). In actuality, the first non-focussing mirror FLARE's pulses hit was replaced by a periscope in order to rotate the polarisation of the pulses by 90° and bring the angle of incidence on the plasma switch closer to Brewster's angle, although hitting the exact Brewster's angle was impractical with this setup. The entire setup after this periscope was raised slightly in order to compensate for the height difference the periscope creates. The first mirror after sideband generation was replaced by a downward periscope to bring the beam back on the spectrometer's level.

4   Results FLARE

While the results of this portion of the project are all connected in that they pertain to the same machine, they can be viewed as more or less separate. Most of them are experimental, but some are a hybrid of simulation and experiment, comparing theory to reality.

Time-Domain Analysis   The processing of the data gathered during the time-domain analysis of FLARE's light required little work. The intensity profiles of pulses at both lasing and non-lasing positions were recorded on a format that was easily graphed using OriginLab's Origin.

A small correction had to be made in the value of the undulator gap and cavity length, however. The performed scans were continuous in reality, but a display of the scanned value often showed duplicates. Additionally, when commencing a scan that would increase either value continuously, the value would often dip down before starting its climb. Lastly, scans would often record several data points on the last value of the scanned variable. This was problematic, as the program would not accept anything but a continuously increasing variable as an axis value. It could only place one pulse profile for every value of the scanned parameter, after all. The dip at the start of the scan and the pause at the end had to be cut off, subsequently, and any duplicate values were eliminated by smoothing the values of the scanned variable using adjacent-averaging.

With these obstacles out of the way, the only matter that remained was the addition of a timescale. This was the one thing not performed automatically and needed to be done based on the pulse length of FLARE. The pulse length was well-defined as it was given by the electron bunch length in the undulator. The upside of adding the second variable of the 3D-graph manually was that there were no duplicate values present by definition.

Performing multiple scans over the undulator gap in the spontaneous emission range of the cavity length, the complete picture can be compared to the earlier shown map of FLARE light intensity mapped as a function of both undulator gap and cavity length.
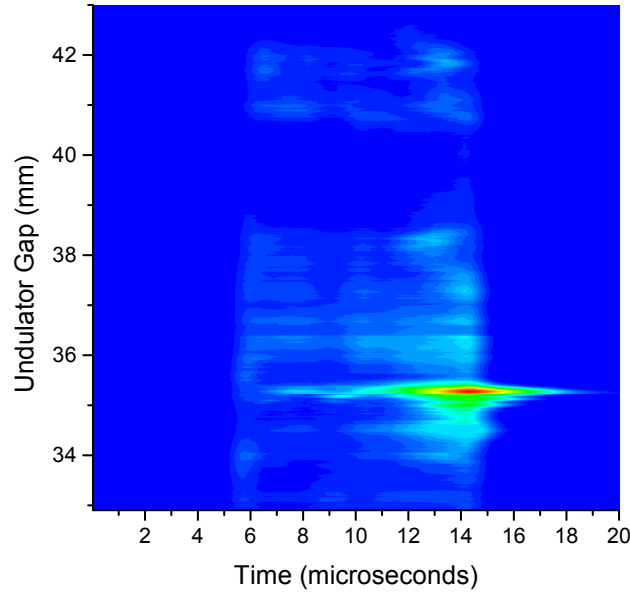

Figure 6: A typical scan performed of the undulator. The cavity length was set to 7518 mm and the undulator gap was scanned over the upper range of FLARE. The cavity length was set well out of lasing range in order to observe spontaneous emission using the sensitive bolometer.

It can be noted in figure 7 that there are regions where spontaneous emission agrees with FLARE lasing. Around an undulator gap of 34 mm there is clear correlation between the two, as well as just below 30 mm and around 27 mm. However, the relation between these graphs is not conclusive. It can be noted that the spontaneous emission around 27 mm is disproportionally strong for its lasing counterpart

at the same undulator setting. Additionally, spontaneous emission continues from 36 mm almost up to 38 mm while this is not observed in lasing. The other way around, lasing does not always imply spontaneous emission. This is best observed around a 39 or 35 mm undulator gap where strong lasing can be found but almost no spontaneous emission is present.

This is a somewhat surprising result. When the downstream mirror is removed and it is assumed that all cavity effects have been sufficiently suppressed, the only thing that is happening is relativistic electron bunches travelling through a waveguided undulator. All of the scanned undulator parameters should in principle be able to produce light and yet clear structures can be seen when the undulator gap is varied in spontaneous emission. This suggests that not well-known effects play a role here, possibly including processes within individual electron microbunches.
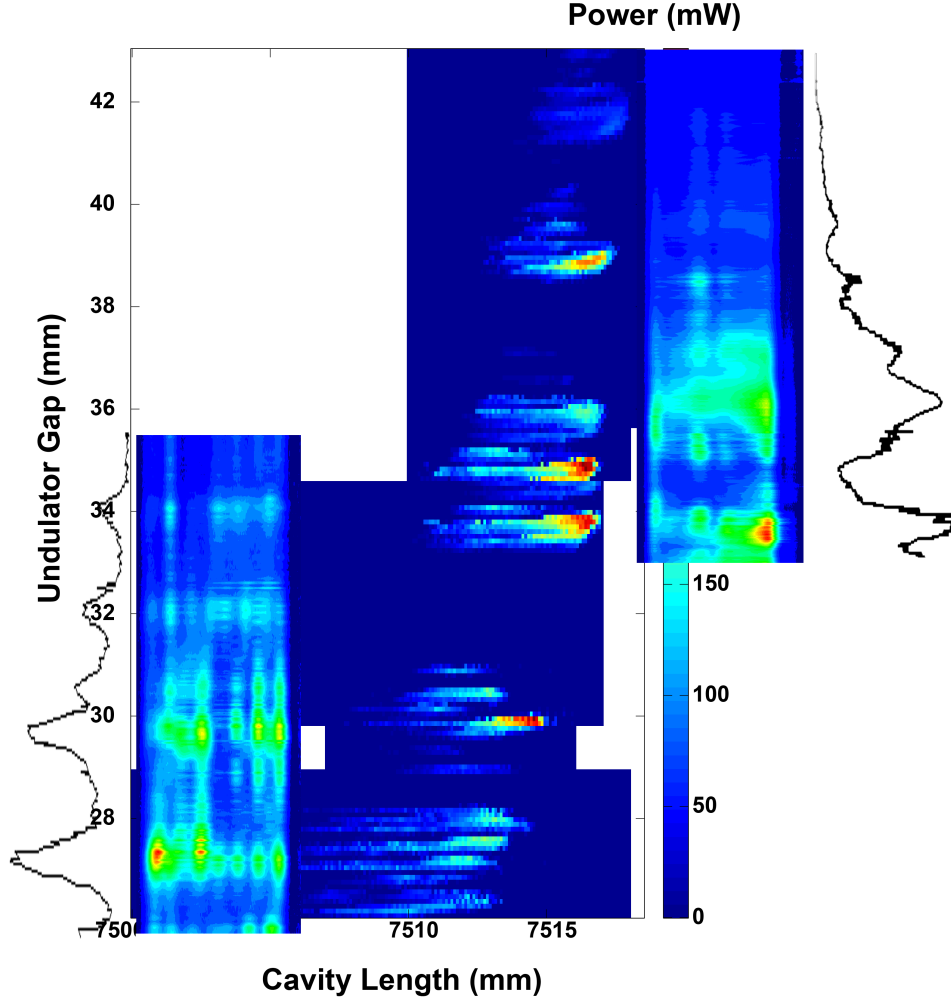

Figure 7: The spontaneous emission scans are overlaid on top of the earlier produced map of FLARE light intensity as a function of undulator gap and cavity length. It must be noted that the horizontal scale of the insets is time rather than cavity length, having a range of 10 μs each. Additionally, the insets each have a vertical line graph which signifies their time-integrated intensity as a function of undulator gap. The vertical scale is shared by all graphs.

Michelson Interferometer Interferograms were only made at specific settings of FLARE thanks to the lengthy nature of their recording. Pulse profiles of light that came out of the interferometer were detected using a bolometer for spontaneous emission and a pyroelectric detector for lasing. Virtual gates were subsequently put around certain sections of the profile that recorded the averages of their designated areas. These averages where then plotted against the displacement of the interferometer's motorised arm to produce interferograms as can be seen in fig 8a and 8b.

It can be noted that the spontaneous emission spectrum is much less clean than the lasing spectrum.

(a) Cavity length: 7520 mm, undulator gap: 28.55 mm

(b) Cavity length: 7513 mm, undulator gap: 28.15 mm

(c) The Fourier-transform of figure 8a.

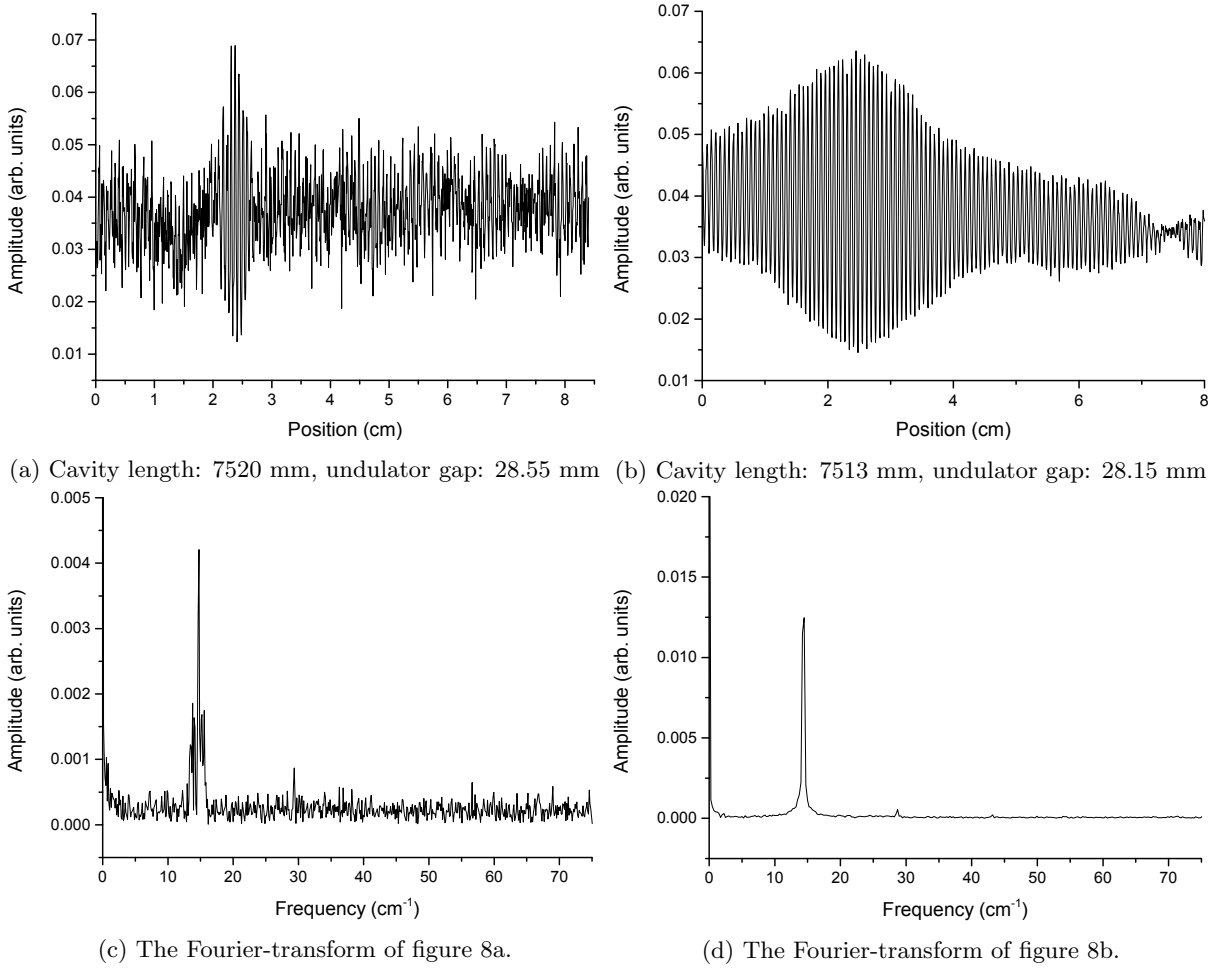(d) The Fourier-transform of figure 8b.

Figure 8: Two interferograms shown side by side along with their respective spectra. The latter are obtained by simple Fourier-transform. The settings of figures 8a and 8c are completely unsuitable for lasing and are thus representations of FLARE's spontaneous emission. Figures 8b and 8d, on the other hand, were taken at settings advantageous to lasing.

This can likely be attributed to two factors: detector noise and the actual FLARE spectrum. Resonant wavelengths and their harmonics exhibit a much weaker signal in spontaneous emission than in lasing, causing other signals such as detector noise to be more prominent in interferograms and, by extension, spectra. Secondly, the spectrum of radiation coming from FLARE is simply expected to be dominated by resonant wavelengths at lasing and less so when emitting spontaneous emission, seeing as they have not been amplified fully in the latter case.

The main wavelength of both the lasing spectrum and the spontaneous emission seems to be just below 15 cm $^{-1}$ and is clearly visible. Second harmonics are also present, however. These should not occur at all in a perfect waveguide and should at least be weaker than the third harmonic in an imperfect one. In normal spectrum characterisation of FLARE, second harmonics appear due to the generation of sideband signals which creates second harmonics of its own, masking FLARE's native second harmonics. Third harmonics are barely visible in the recorded spectra.

Theoretical Analysis of Waveguide Dispersion Equation 2 is most conveniently written as a function of the undulator parameter K as this reflects FLARE's operation in the real world. Rewriting the equation in terms of K yields

$$\nu_{n,m}(K) = \frac{c\gamma^2\epsilon_m}{l_0(1+K^2)}\left(1 \pm \sqrt{1 - \left(\frac{nl_0\sqrt{1+K^2}}{2b\gamma\epsilon_m}\right)^2}\right) \quad , \quad \epsilon_m = 1 - (m+1/2)/k_0 z_r \qquad (5)$$

13

Note that the factor β_z has been left out of this equation as it is sufficiently close to unity to be of negligible influence. Additionally, the $\pm$ has been replaced with a plus-sign in order to purely regard the high frequency branch in the waveguide dispersion. The low frequency branch is hereby disregarded.

Firstly, the order of the Hermite-Gaussian modulation m was varied in order to observe its effects. In reality, this factor only takes on small integer values, starting at a value of 0. Likewise, n is also assumed to only take on small integer values, starting at a value of 1, in contrast. The frequency seemed to be hardly affected at all by variation of m, however, as demonstrated in figure 9.
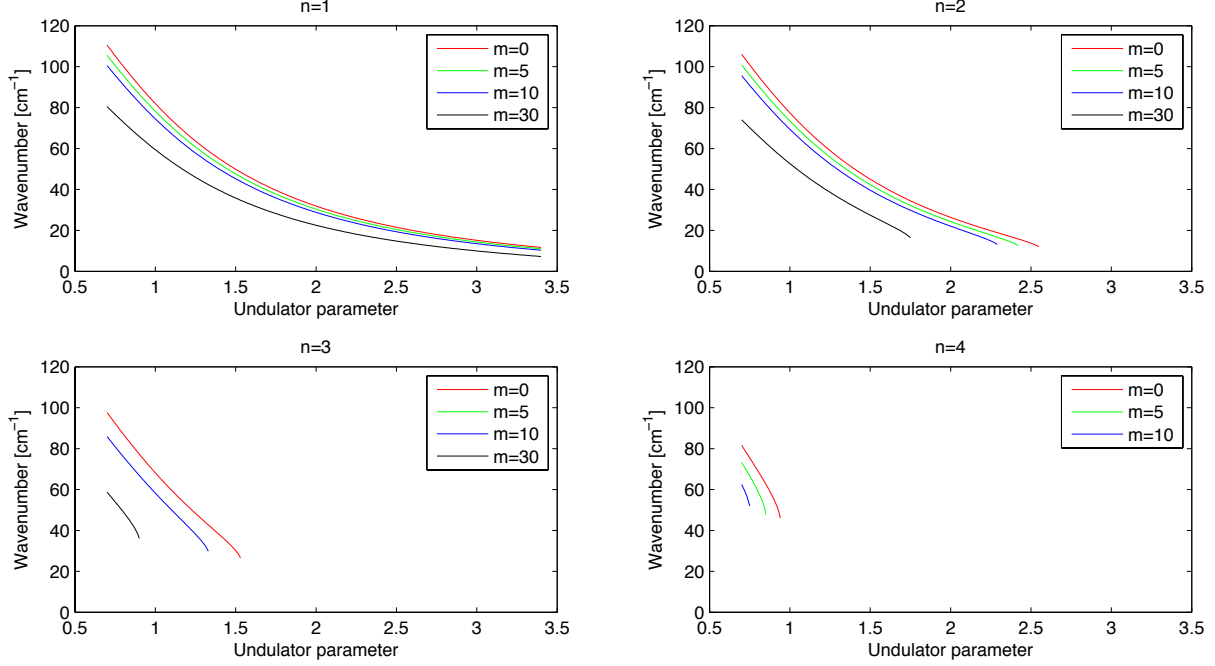

Figure 9: The produced radiation wavenumber as a function of undulator gap for multiple values of n and m. The kinetic energy of the electrons in all cases was chosen to be 15 MeV.

It can be noted that hardly any notable change occurs even when m takes on the already-high value of 5. Real changes only occur for ridiculously high values. What can be taken away from this is that variation in m is hardly of importance for realistic values and can be set to zero to somewhat simplify the equation.

Keeping the same values for n and setting m to zero, the dependence on the electron's kinetic energy can be investigated. This value comes into the equation by

$$E_k = (\gamma - 1)m_e c^2 \quad \Rightarrow \quad \gamma = \frac{E_k}{m_e c^2} + 1 \tag{6}$$

Here, E_k signifies the kinetic energy of the electron and m_e its mass. Together with the speed of light c, they define the γ of the electrons fully. FLARE is commonly run at $E_k = 10$, 15 and 16 MeV and these vaues were subsequently used to simulate additional curves, along with an intermediate value of 13 MeV. The results can be seen in figure 10.

Differences between these graphs are much more appreciable than those in figure 9. Sending electrons with different kinetic energy through the undulator makes a large difference in the wavelength of the produced radiation. Focussing and guiding of the electron beam is dependent on its energy and thus changes in electron energy are made step-wise, while changes in the undulator gap can be made continuously. Focussing on the strongest of the harmonics, namely $n = 1$, it can be seen that the longest wavelengths can more comfortably be reached with a lower electron energy. An increase in electron kinetic energy results in a sharp incline towards higher frequencies at low undulator gaps, however.

In all of the results, it can be noted that the energy difference between different harmonics at any given undulator parameter is substantial. This large energy difference would imply that radiation can not easily switch between harmonics and thus any n values present in the spectrum will likely have been amplified from an earlier stage rather than added to later on. Additionally, curves discussed here often
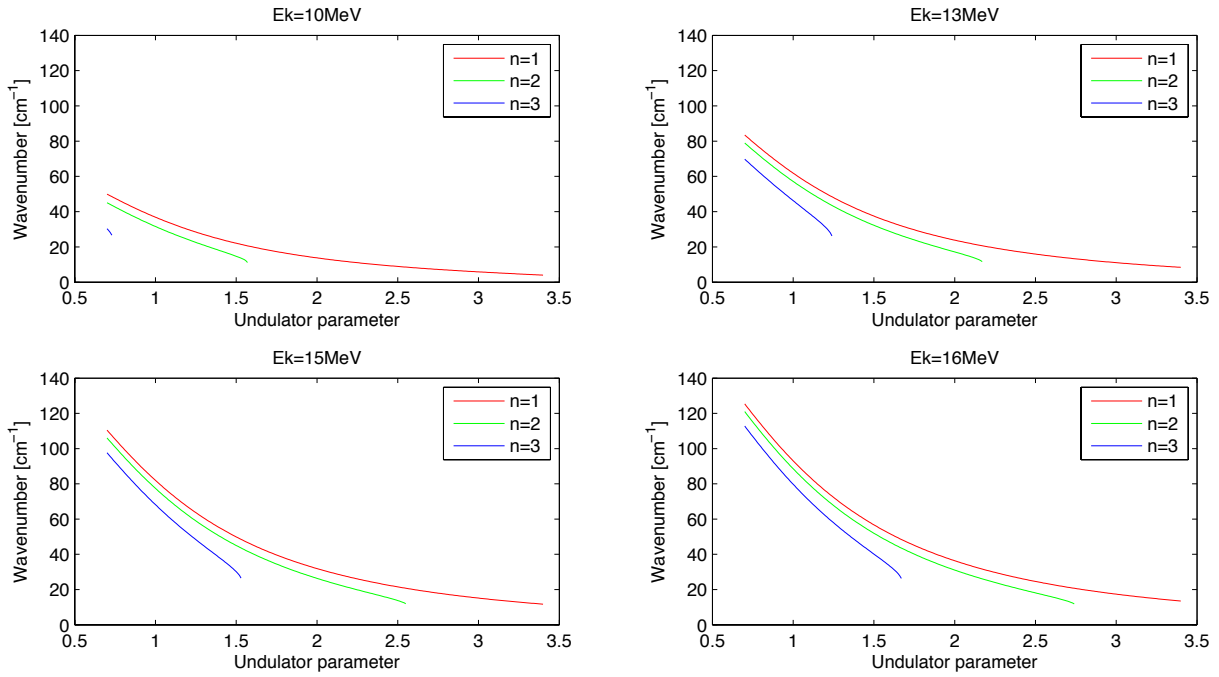
14

Figure 10: Curves representing the produced wavenumber as function of the undulator parameter and electron kinetic energy. m was set to zero in all cases.

have an end. Beyond the cut-off undulator parameter, the term under the square root in equation 5 becomes negative, requiring the frequency of that specific mode to have an imaginary component in order to propagate through the waveguide.

Theoretical Analysis of the Electron Bunch Shape   Even though the entire electron microbunch is only around 10 ps long, intrabunch effects play a large role in achieving lasing. As detailed in an earlier written theoretical thesis on FLARE gain (see also [7] and [12]), microbunching is influenced by a previously built-up weak electromagnetic field and greatly enhances the coherent emission of an electron bunch. Likewise, electron bunches that have a disadvantageous shape coming into the undulator can severly interfere with the production of the appropriate spontaneous emission that is paramount to future lasing.

Equation 3 and 4 show that the effect of a certain pulse shape can mean dominance of coherent emission over incoherent emission, or the other way around. A uniform electron beam implies a constant longitudinal density distribution and a suppressed coherent emission. This is mediated through the form factor, compensating for the extra factor N in the coherent term which is generally very large.

A smooth gaussian with a standard deviation of $3 \cdot 10^{-12}$ s (approximately $9 \cdot 10^{-4}$ m) can be examined as a test case. The form factor can then be determined as follows:

$$S(t) = \frac{1}{\sigma} \exp\left(-\frac{t^2}{2\sigma^2}\right) \quad \Rightarrow \quad f(\omega) = \exp\left(-\omega^2 \sigma^2\right) \tag{7}$$

Here, σ signifies the standard deviation. Note that S has been written as a function of time t instead of longitudinal position z. The conversion factor for this is the speed of light c, or more accurately the longitudinal velocity of the electron beam v_z. This results in a form factor as a function of frequency ω rather than wave vector k.

The power of an individual electron P_1 is likewise dependent on the frequency, following the profile of a sinc function as follows [1]:

$$P_1(\omega) = \left| \mathrm{sinc}\left(\frac{Q(\omega)L}{2}\right) \cdot \exp\left(i\frac{Q(\omega)L}{2}\right) \right|^2 \quad , \quad Q(\omega) = \frac{\omega}{v_z} - \left(k_0 + \frac{\omega}{c}\right) = \omega \frac{c - v_z}{v_z c} - k_0 \tag{8}$$

It can be seen here that the minute difference between the longitudinal velocity of the electron bunch and the speed of light does make a difference at sufficiently high frequencies as it effectively acts as a correction

15

on the undulator wave vector $k_0 = 2\pi/l_0$ and effectively creates a resonance condition, as can be seen in figure 11.
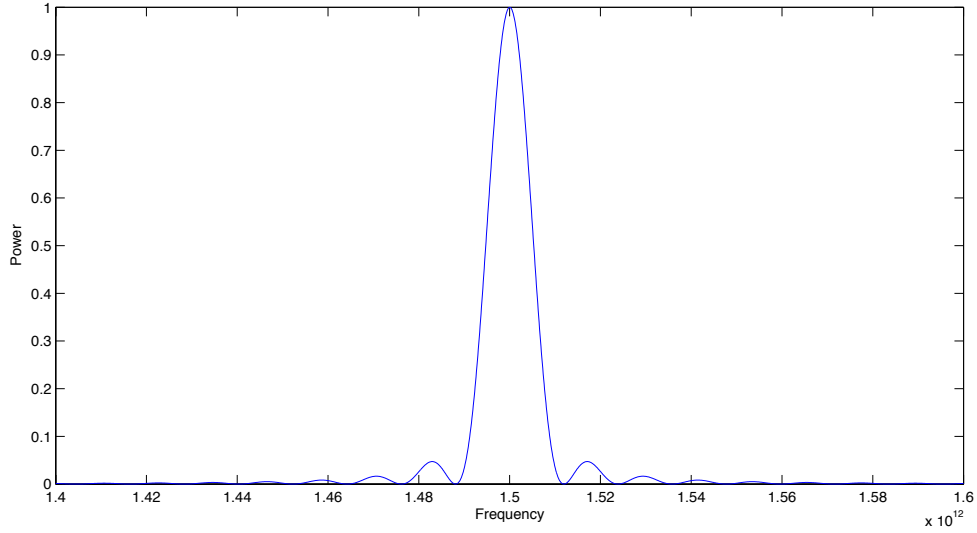

Figure 11: The normalised power spectrum for a single electron with $v_z = 0.988713 \cdot c$.

P_1 takes on a maximum when $Q(\omega) = 0$, which means that $\omega = \frac{k_0 v_z c}{c - v_z}$ at the apex of a single electron's power output. This means that the longitudinal velocity of the electrons single-handedly fixes the lasing frequency.

A combination of all the previously discussed factors yields the coherent and incoherent terms of the total power equation. Since N is generally very large and in the case of FLARE takes on the value of 10^9, dominance between the two terms switches extremely rapidly.
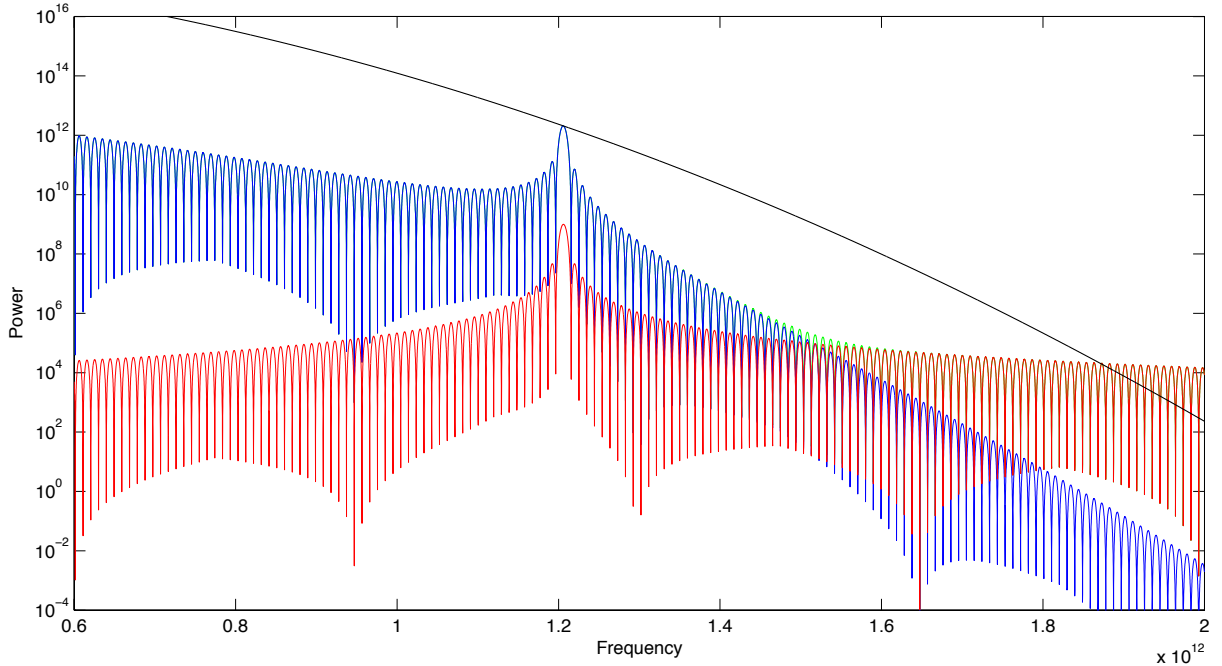

Figure 12: Coherent spontaneous emission (blue), incoherent spontaneous emission (red) and total spontaneous emission (green) as a function of frequency with $v_z = 0.986 \cdot c$. The black line denotes $N^2 f(\omega)$, revealing the effect the form factor has on the coherent spontaneous emission.

The coherent spontaneous emission initially benefits greatly from the extra factor N, but quickly falls below the incoherent spontaneous emission thanks to the frequency evolution of the form factor.

16

The dominance of much lower frequencies over the resonant frequency thanks to the shape of the form factor are mostly not of importance, as the waveguide and laser cavity do not allow sustainable buildup of radiation at this range. Note that the total spontaneous emission follows the dominant term closely. The vertical scale has been chosen somewhat arbitrarily, seeing as the individual electron power has been normalised. These experiments are only concerned with a qualitative analysis of the spontaneous emission and thus the exact value of the produced power is relatively unimportant.

A differently shaped electron bunch can be simulated with the addition of a second gaussian. This creates a slightly broader profile, depending on the distance between the gaussian curve. The form factor subsequently becomes:

$$f(\omega) = \frac{1}{2} \exp\left(-\frac{\sigma\omega(\sigma\omega + in)}{2}\right) \cdot (1 + \exp(in\sigma\omega)) \tag{9}$$

Here, n denotes the amount of standard deviations the two gaussians are apart. The factor $\frac{1}{2}$ is there merely for normalising purposes. With all other factors unchanged relative to the test case, n can be set to the not quite random value of 0.877 at an electron longitudinal velocity of $0.9889 \cdot c$, implying a temporal distance between the two gaussians of $2.63 \cdot 10^{-12}$ s. The result of these values can be seen in figure 13
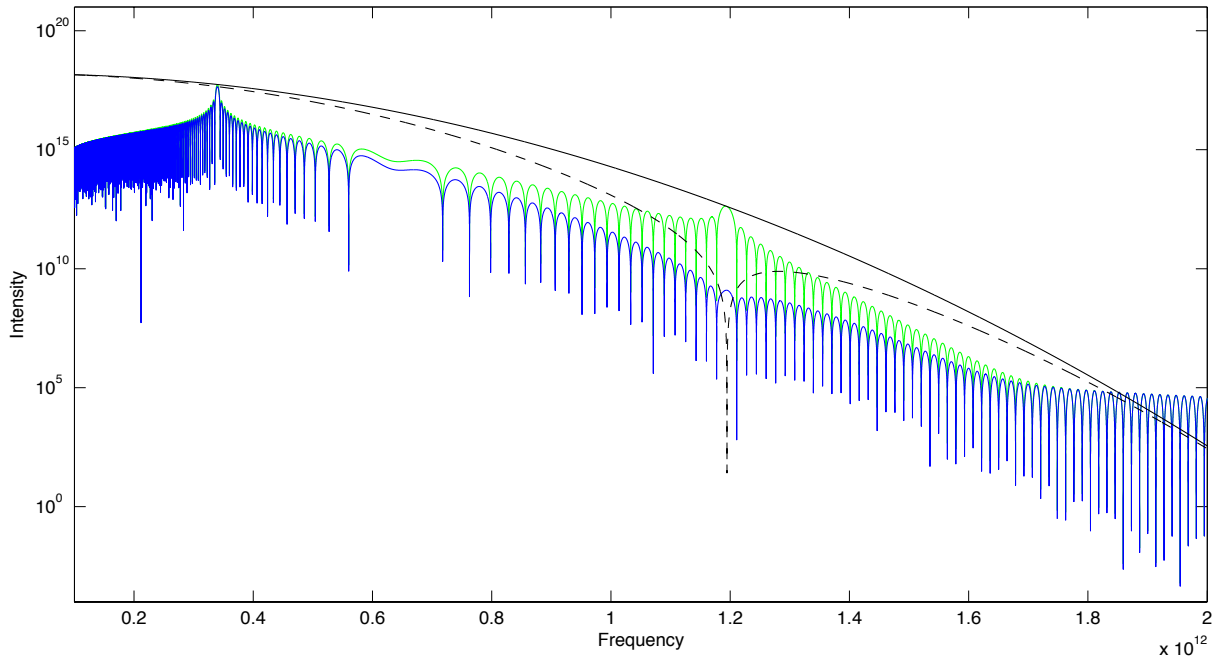

Figure 13: The power spectrum of two gaussians at a distance of $2.63 \cdot 10^{-12}$ s (blue), that of a single gaussian (green) and the form factors of a single and double gaussian (black and black dotted, respectively).

It can immediately be seen that a double gaussian at the appropriate distance greatly suppresses the resonant peak. This is due to the fact that the bunches are located half a resonant wavelength apart, destructively interfering. The same process occurs to a lesser degree when the spacing does not exactly equal half the resonant wavelength as can be seen by the dip in the black dotted curve.

The low frequency branch is also clearly visible and much stronger than the high frequency branch in either case. However, the low frequency branch is not amplified properly in the laser cavity due to differing group velocities and a subsequent mismatch between light pulses and electron bunches, rendering the problem harmless. With a disadvantageous bunch shape such as the one demonstrated in figure 13, on the other hand, even non-resonant frequencies near resonance are more intense than the original peak. This becomes even more apparent when observing the new form factor: a sharp dip clearly indicates the influence of destructive interference.

The shape of the electron microbunch in the undulator could thus present problems for lasing. While smooth gaussian bunch profiles pose little problems, a combination of peaks may generate undesirable effects, possibly stopping the process of lasing in its tracks.

5 Results THz Pulse Slicing

Detection and Laser Testing   In order to characterise the nanosecond resolution detector and Nd:YAG pumping laser, a short test was carried out. The laser is tunable in power output, but was let run near full power for some minutes in order for its pulses to stabilise. Reflective neutral density filters were applied to the detector in order to protect it from the intense light and a beam dump was set up in order to safely dispose of the reflected pulses.
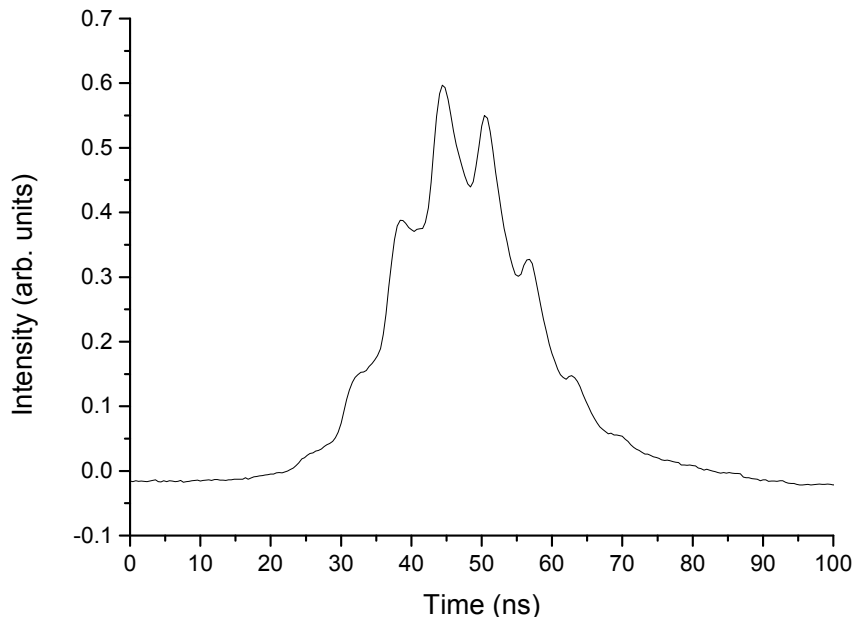

Figure 14: A scan of the Nd:YAG laser pulse's temporal profile.

It can immediately be seen that the advertised 10 ns long pulse is in actuality more than 30 ns long. This is still short enough for the purpose of these experiments, however. Multiple smaller peaks can easily be observed in the general profile: a testament to the detector's temporal resolution.

Analysis   Experiments were conducted on all three types of plasma switches: 5 μm SOI, 20 μm SOI and bulk silicon. Of these, portions with and without reflective coating were examined in order to determine their effect. All six of these areas were characterised with regards to different wavelengths of FLARE. At each specific area and FLARE wavelength, a series of measurements was conducted with differing YAG pumping power, starting at saturation and gradually going down.

Measurements were taken with zero YAG pumping power, as well as measurements with an almost perfectly reflecting mirror in place of the plasma switch. Both of these serve as references: a measurement without YAG pumping reveals the inherent reflectivity of the plasma switch and can be subtracted from the main experiment to yield the reflectivity that was added by the YAG pumping. A measurement involving a perfectly reflecting mirror can then be used to normalise the added reflectivity, compensating for FLARE pulse shapes and other fluctuations. The three types of measurements can be observed in figure 15.

During analysis, it appeared that the reflectivity occasionally dipped below the inherent reflectivity, causing a negative added reflectivity as can clearly be seen in figure 16. This is an unknown mechanism that was absent in previous experiments that utilised an angle much closer to Brewster's angle than was possible here. It is assumed that an unknown absorbing effect takes place from the moment the pumping laser strikes the plasma switch. This new effect could be considered constant in many cases, but in some has been regarded as a linearly waning factor. For the purposes of this experiment, the entire curve was lifted with a certain factor if it dipped below zero at any point.

Power-dependent measurements were carried out for on all areas for FLARE wavelengths of 360 μm, 465 μm, 700 μm and 783 μm. From these, the power-dependence of the reflectivity could be derived. For this purpose, the first half microsecond of each curve was average in order to determine an average maximum reflectivity. These power-dependence measurements were discarded over earlier performed measurements
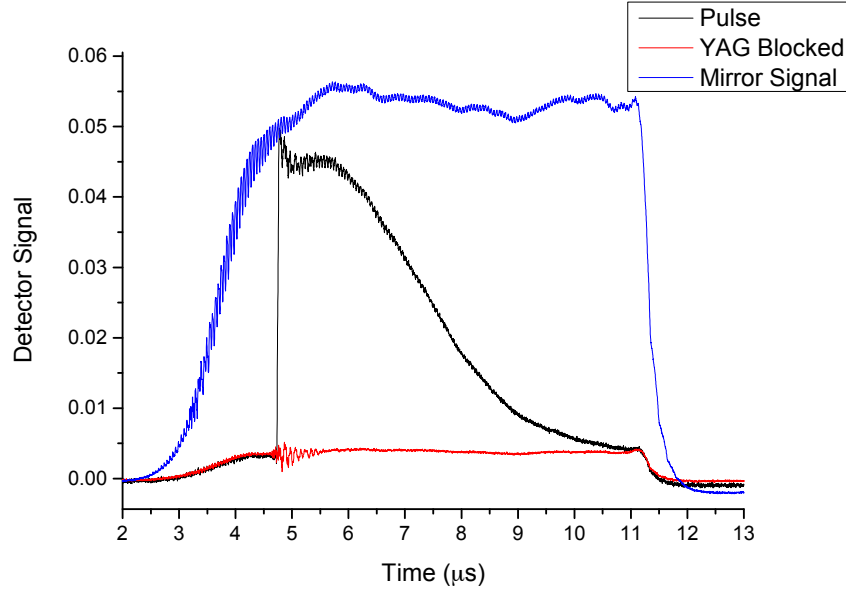
Figure 15: A raw measurement (black) graphed with the inherent reflectivity (red) and a perfectly reflecting mirror (blue). The inherent reflectivity is subtracted from the raw measurement, after which the result is divided by the perfect reflection for normalising purposes. The vertical scale is therefore an arbitrary one.
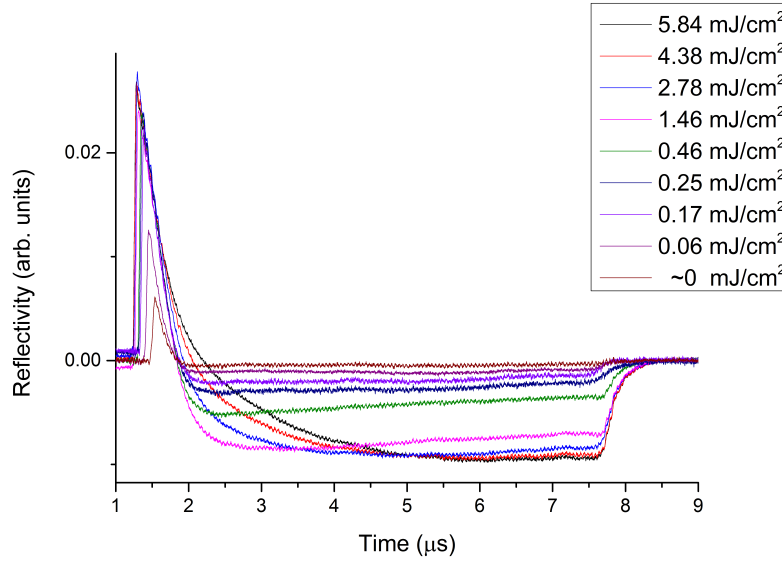

Figure 16: A series of measurements in which the reflectivity clearly dips below zero. The energy per pulse per area is given for every curve.

with more data points, in the end. As can be observed in figure 17, they do not correspond completely. While bulk reflectivity is dominant for 700 μm and 360 μm, it is not so for 465 μm where it is swapped with the 20 μm SOI mirror.

Comparisons between areas coated with anti-reflectivity and passivation coating, and those without were made for the 5 μm SOI and bulk mirrors. This coating prolongs the reflecting qualities of the plasma switch by reducing surface recombination of charge carriers and should thus make for longer-living reflectivity. This was indeed observed for all FLARE wavelengths, as can be seen in figure 18 for one specific wavelength. Notice that the peak reflectivity stays virtually the same while the decay is impeded by the coating.
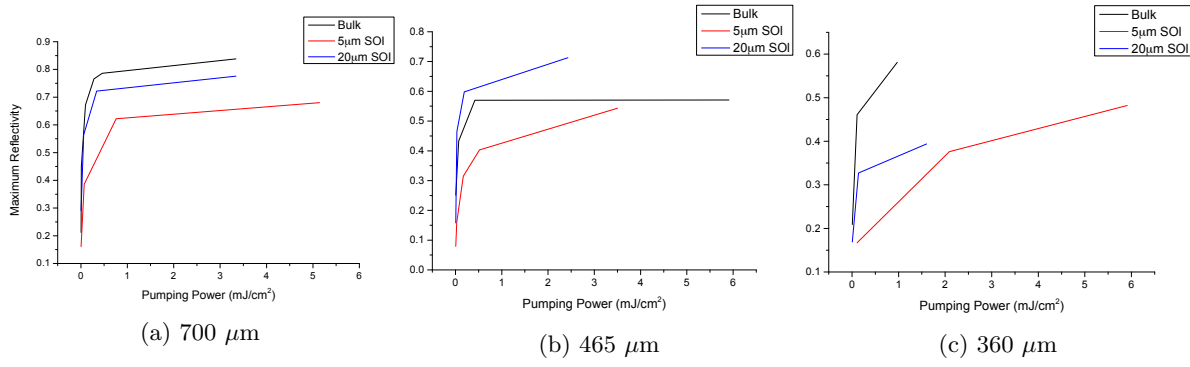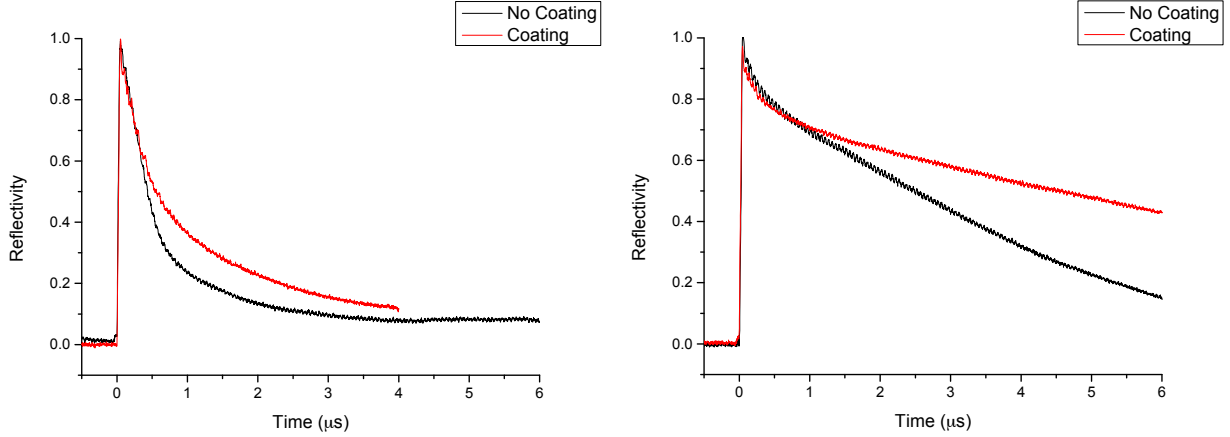
(a) 700 μm   (b) 465 μm   (c) 360 μm

Figure 17: Power-dependence measurements for various FLARE wavelengths and all plasma switches.

(a) Time evolution of 5 μm SOI mirror reflectivity, coated and uncoated.

(b) Time evolution of bulk silicon mirror reflectivity, coated and uncoated.

Figure 18: Comparisons between coated and non-coated plasma switches at a FLARE wavelength of 700 μm.

Comparison to Simulation Models   The recorded and processed reflection curves can be loaded into MATLAB in order to fit them to simulation models. Since all of the plasma switches are assumed to have the same material properties, they were simulated using identical fitting parameters. Initially, experimental data was compared to simulations with parameters that had fit previous experiments. They can be seen in figure 19.

It can be noticed that all of the simulations are longer-lived than the experimental results. Additionally, while the shape of the 20 μm SOI plasma switch experimental results correspond with that of its accompanying simulations, the shape of the 5 μm SOI and bulk silicon mirror differ greatly in shape from their counterparts. This may be attributed to the fact that previous experiments on which these simulations were based utilised a detector that could not resolve the exact temporal profile of the mirrors' reflectivity. A sharp peak such as those produced by the 5 μm SOI mirror is broadened and fits the current simulation nicely. The low amplitude of the shorter wavelength experimental data may be attributed to absorption by water in the air.

Altering the fitting parameters in order to better fit the experimental results helps somewhat. Surface recombination effects have more influence on thinner SOI mirrors and bulk recombination has a larger impact on thicker plasma switches. This suggests that the surface recombination rate is actually higher than previously thought and the bulk recombination is lower.

These simulations featuring the new parameters fit the experimental data better, as can be seen in figure 20. The 5 μm SOI mirror simulation has been made shorter-lived and the bulk silicon mirror longer. This goes at a cost, however. The defect recombination rate had to be set to zero in order for the bulk silicon curve to have the correct decay rate while retaining the short reflectivity of the 5 μm SOI mirror. Meanwhile the front surface recombination has taken on a value beyond credibility: 5000 cm/s. Giving up the match between the shapes of the curves and instead going for proximity, the back surface
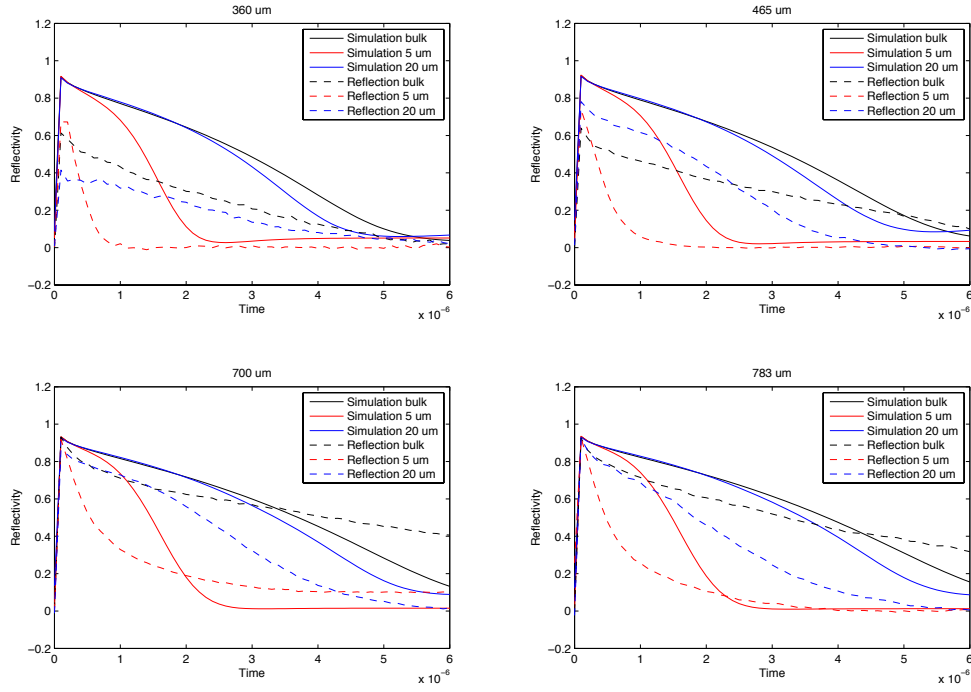
20

Figure 19: The simulations (solid lines) and experimental results (dotted lines) of the plasma switches for various FLARE wavelengths. Fitting parameters used here are as follows. Front surface recombination: 50 cm/s, back surface recombination: 1500 cm/s, defect recombination rate: $6 \cdot 10^5$ s^{-1}.
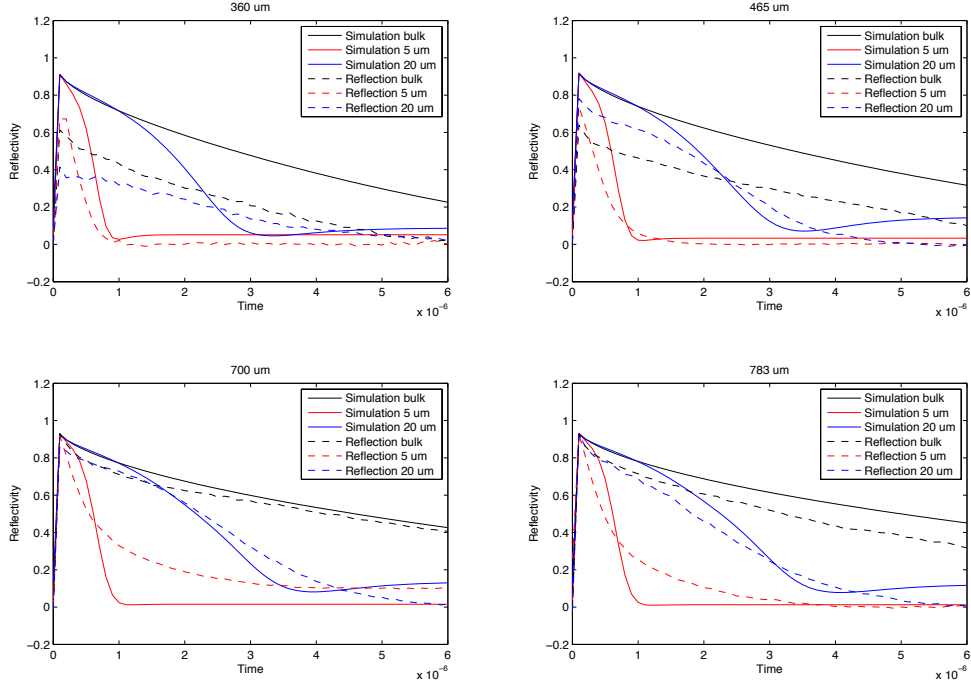

Figure 20: Once again the simulations (solid lines) and the unchanged experimental values (dotted lines) of the plasma switches for various FLARE wavelengths. The altered fitting parameters are as follows. Front surface recombination: 5000 cm/s, back surface recombination: 1500 cm/s, defect recombination rate: 0 s^{-1}.

recombination can be increased instead of that of the front surface.

It can be seen in figure 21 that the bulk silicon mirror simulations no longer match their experimental counterparts in shape, but the fitting parameters are much more acceptable. The 5 μm SOI mirror
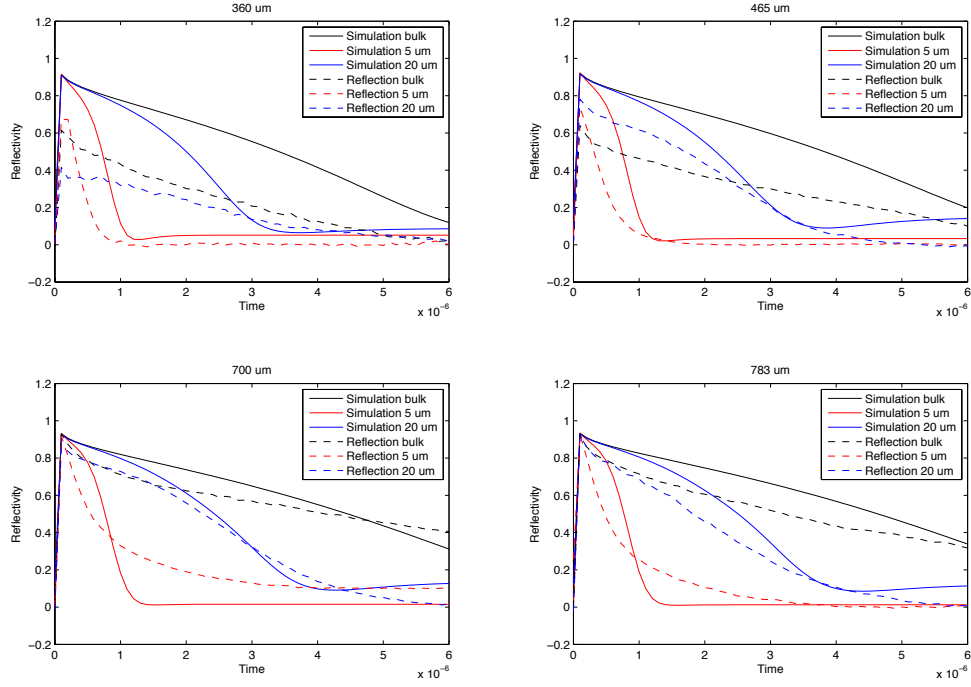
Figure 21: A second attempt at fitting the simulation to the experimental data. Front surface recombination: 500 cm/s, back surface recombination: 4000 cm/s, defect recombination rate: $4 \cdot 10^5$ s^{-1}.

simulations remain problematic in all cases, however, unable to obtain the initial sharp peak nor the smooth decay that can be seen with the longest two FLARE wavelengths. Additionally, none of the 20 μm display the final rise in reflectivity that all the simulations offer.

All in all, the simulations do not differ greatly from wavelength to wavelength while the experimental data does. This might signify a shortcoming in the experiment, but it is likely that the simulations are incomplete and could be improved upon in the future.

6   Conclusion

FLARE   When a complex machine does not function according to plan, it can be very difficult to find the defect. The error could be buried deep in the inner workings of the apparatus and it could be a combination of many small factors. In these cases where the problem is far out of sight and hunches drive further experiments, it is instrumental that as much data is gathered as possible and presented in a clear and intuitive way in order to find a pattern and to find a reason.

While FLARE's intensity map as a function of undulator gap and cavity length was already made, the spectrum of FLARE at positions in this graph was relatively unknown. While sideband generation allowed for lasing output to reveal its spectrum through a spectrometer, a Michelson interferometer was required to characterise the much weaker spontaneous emission. Spectra were determined of FLARE lasing and non-lasing in its normal operation, as well as spontaneous emission when the downstream mirror of the laser cavity was blocked and later removed. Aside from these spectra, temporal profiles of FLARE's pulses were recorded with a sensitive bolometer in order to examine, in extension, the shape of the electron bunch in the undulator.

In less experimental circumstances, the waveguide dispersion was made visible. It was examined how the output frequency changes relative to certain factors, always as a function of the undulator parameter. These curves may be used to find determine whether modes differing from the desired one are disrupting the lasing process of FLARE. Additionally, electron bunch analysis was performed in order to ascertain that certain double-peaked electron bunch shapes could disrupt spontaneous emission from forming properly.

Pulse Slicing Mirrors   While FLARE produces a special kind of light that effectively bridges the THz gap, its pulses are rather long. In order to perform certain dynamic experiments, short pulses or a series of short pulses is required. These cannot be made in the laser cavity itself and thus plasma switches find their use in this context.

A large series of experiments was conducted on three types of pulse slicing mirrors: 5 μm and 20 μm SOI mirrors and a bulk silicon mirror. The power dependence of their maximum reflectivity was determined and it was confirmed that the passivation layer works as intended by diminishing the surface recombination rate.

Finally, the experimental data was compared to simulation models. Fitting parameters were used to attempt the creation of a match between theory and experiment. This was only partially successful. The fitting parameters need to take on values very far from the previously optimised ones if the simulations are to come close to experimental values. Nonetheless, the pulse slicing mirrors work more or less as previously determined and especially the 20 μm seems suited for FLARE pulse slicing thanks to its moderately long reflectivity retention. Multiple pulse slicing mirrors could be used in tandem to slice pulses multiple times and achieve the desired temporal profile for new dynamic experiments.

7   Discussion and Future Improvements

FLARE   Although this experiment has brought new insights to life concerning the scanning problems of FLARE, solutions to the general scanning problem have been in short supply. The time-domain analysis of spontaneous emission showed that spontaneous emission does not imply lasing, nor does lasing imply strong spontaneous emission. More experiments could be carried out in the future to investigate the spontaneous emission both temporally and spectrally.

Continuing on the topic of spontaneous emission, theoretical analysis of two-peaked electron microbunches travelling through the undulator have shown to be able to extinguish extinguish crucial wavelengths in the spontaneous emission. Analysing the exact shape of FLARE's electron bunches and determining whether they have this problem to any degree might be one of the first steps towards solving the scanning problem. Observing individual microbunches is no small feat, however, since their length is on the order of 10 ps.

Pulse Slicing Mirrors   The various plasma switches have been characterised and compared to existing simulation models. A fundamental mismatch is visible between theory and experiment that cannot be solved by the use of fitting parameters. While the general shapes of the 20 μm SOI and bulk silicon mirror can be approximated by applying large changes to the fitting parameters, the general picture remains unsatisfactory. Future simulation models could build on the gathered results in order to provide a more complete picture of the plasma switches' exact workings.

Experimentally, improvements can also be made. One of the main problems that arose during these experiments was the tendency of the mirrors to take on reflectivities lower than their inherent reflectivity. This caused the added reflectivity to take on negative values. A solution for this would have been to work at Brewster's angle. Since the inherent reflection of the plasma switches is zero under this angle, any reflection that is detected during experiments will be positive.

Lastly, the YAG laser causes some small interference as can be seen particularly well in figure 15. The profile of the inherent reflectivity clearly shows disruptions as the blocked YAG laser fires. Although this is not a problem when experiments can be taken in quick succession, it should be taken in consideration for long experiments since the fluctuations have been observed to deform over long periods of time.

References

[1] David T. Attwood. *Soft X-rays and Extreme Ultraviolet Radiation: Principles and Applications.* Cambridge University Press, 2000.

[2] Encyclopædia Brittanica. Interferometer (instrument).

[3] Ramian G. Hu J. Amir A. Elias, L.R. Observation of single-mode operation in a free-electron laser. *The American Physical Society - Physical Review Letters Volume 57, Number 4*, 1986.

[4] Research Facility for Science and Technology Tokyo University of Science. Principle of free electron laser (fel).

[5] Bakker R.J. van der Meer A.F.G. Oepts D. van Amersfoort P.W. Jaroszynski, D.A. Coherent startup of an infrared free-electron laser. *The American Physical Society - Physical Review Letters Volume 71, Number 23*, 1993.

[6] van der Zande W.J. van der Meer A.F.G. Lehnert U. Michel P. Wünsch R. . . . van der Slot P.J.M. Jongma, R.T. Design of the nijmegen high-resolution thz-fel. 2008.

[7] Thomas C. Marshall. *Free-Electron-Lasers.* MacMillan Publishing Company, 1985.

[8] Radboud University Nijmegen Faculty of Science. Fel operating principle - general description.

[9] Spectra-Physics. Quanta-ray indi.

[10] Thorlabs. High-speed photodetectors.

[11] Berden G. Jongma R.T. Wijnen, F.J.P. A simple optical spectral calibration technique for pulsed thz sources. *Optics Express*, 2010.

[12] Amnon Yariv. *Quantum Electronics.* John Wiley & Sons, Inc., 1988.